The Astrophysical Journal, 948:92 (14pp), 2023 May 10 https://doi.org/10.3847/1538-4357/acbf1e

JWST Observations of the Enigmatic Y-Dwarf WISE 1828+2650. I. Limits to a Binary Companion

Matthew De Furio[1], Ben Lew[2,3], Charles Beichman[4,5], Thomas Roellig[3], Geoffrey Bryden[5], David Ciardi[4,5], Michael Meyer[1], Marcia Rieke[6], Alexandra Greenbaum[7], Jarron Leisenring[6], Jorge Llop-Sayson[8], Marie Ygouf[5], Loic Albert[9], Martha Boyer[10], Daniel Eisenstein[11], Klaus Hodapp[12], Scott Horner[3], Doug Johnstone[13,14], Doug Kelly[6], Karl Misselt[6], George Rieke[6], John Stansberry[10], and Erick Young[15]
[1] Department of Astronomy, University of Michigan, Ann Arbor, MI 48109, USA; defurio@umich.edu
[2] Bay Area Environmental Research Institute, Moffett Field, CA 94035, USA
[3] MS 245-6, NASA Ames Research Center, Moffett Field, CA 94035, USA
[4] NASA Exoplanet Science Institute, Infrared Processing and Analysis Center (IPAC), Pasadena, CA, USA; chas@ipac.caltech.edu
[5] Jet Propulsion Laboratory, California Institute of Technology, Pasadena, CA 91125, USA
[6] Steward Observatory, University of Arizona, Tucson, AZ 85721, USA
[7] IPAC, Caltech, 1200 E. California Blvd., Pasadena, CA 91125, USA
[8] California Institute of Technology, 1200 E. California Blvd., Pasadena, CA 91125, USA
[9] Université de Montréal, Montréal, Quebec H3C 3J7, Canada
[10] Space Telescope Science Institute, 3700 San Martin Drive, Baltimore, MD 21218, USA
[11] Harvard-Smithsonian Center for Astrophysics, 60 Garden St., Cambridge, MA 02138, USA
[12] University of Hawaii, Hilo, HI 96720, USA
[13] NRC Herzberg Astronomy and Astrophysics, 5071 West Saanich Rd., Victoria, BC, V9E 2E7, Canada
[14] Department of Physics and Astronomy, University of Victoria, Victoria, BC, V8P 5C2, Canada
[15] Universities Space Research Association, 425 3rd St. SW, Suite 950, Washington, DC 20024, USA
Received 2022 December 1; revised 2023 February 19; accepted 2023 February 21; published 2023 May 10

Abstract

The Y-dwarf WISE 1828+2650 is one of the coldest known brown dwarfs with an effective temperature of ∼300 K. Located at a distance of just 10 pc, previous model-based estimates suggest WISE1828+2650 has a mass of ∼5–10 M_J, making it a valuable laboratory for understanding the formation, evolution, and physical characteristics of gas giant planets. However, previous photometry and spectroscopy have presented a puzzle, with the near impossibility of simultaneously fitting both the short- (0.9–2.0 μm) and long-wavelength (3–5 μm) data. A potential solution to this problem has been the suggestion that WISE 1828+2650 is a binary system whose composite spectrum might provide a better match to the data. Alternatively, new models being developed to fit JWST/NIRSpec, and MIRI spectroscopy might provide new insights. This article describes JWST/NIRCam observations of WISE 1828+2650 in six filters to address the binarity question and to provide new photometry to be used in model fitting. We also report adaptive optics imaging with the Keck I0 m telescope. We find no evidence for multiplicity for a companion beyond 0.5 au with either JWST or Keck. Companion articles will present low- and high-resolution spectra of WISE 1828 obtained with both NIRSpec and MIRI.

Unified Astronomy Thesaurus concepts: Brown dwarfs (185); Y dwarfs (1827); Visual binary stars (1777); Binary stars (154); James Webb Space Telescope (2291); Theoretical models (2107); Infrared spectroscopy (2285)

1. Introduction

The WISE mission (Wright et al. 2010) identified cool brown dwarfs (BDs) using their very red ([3.4]–[4.6] or hereafter W1–W2) colors (Kirkpatrick et al. 2011). The most extreme of these objects, with effective temperatures $T_{\rm eff}$ <500 K, have been typed as Y dwarfs (Cushing et al. 2011; Kirkpatrick et al. 2012). With W1–W2 > 4.2 mag, WISEP J182831.08 + 265037.8 (hereafter WISE 1828+2650) was identified as one of the reddest of this small group of only two dozen Y dwarfs. Follow-up photometry and spectroscopy with the Hubble Space Telescope (HST), the Spitzer Space Telescope, and various ground-based facilities found weak emission between 1.0 and 1.7 μm marked by absorption due to H_2O, CH_4, and NH_3 (Cushing et al. 2011), as well as extremely weak emission in the K band (2.2 μm), followed by a sharp rise out to 5 μm.

Astrometry from Keck, Spitzer, and HST determined distances to the WISE Y-dwarf sample ranging from 5 to 15 pc (Beichman et al. 2013; Martin et al. 2018; Kirkpatrick et al. 2019). With distances serving to constrain the absolute luminosity and typical ages of 3–10 Gyr inferred from their transverse motions, it was possible to fit the photometry and spectroscopy to evolutionary models to estimate masses from 5 to 10 M_J. Beichman et al. (2014) and Kirkpatrick et al. (2019) put WISE 1828+2650 at a distance of 9.93 ± 0.23 pc and suggested an effective temperature of 400 K and a mass around 5 M_J.

WISE 1828+2650 has proven to be exceptional even within the unusual class of Y dwarfs. Its extreme W1–W2 color, the difficulty in simultaneously fitting models to the 1–2 and 3–5 μm photometry, and WISE 1828+2650's position at least 1 mag above the Y/T dwarf locus in the H–W2 color–magnitude diagram (Kirkpatrick et al. 2019, Figure 8) have highlighted the challenges of making satisfactory models for such cold objects. Leggett et al. (2013, 2017) suggested that WISE 1828+2650

Table 1
JWST NIRCam Observing Parameters (PID:#1189)

Instrument	Filter Pair	Readout	Groups/Int	Ints/Exp	Dithers	Total Time (s)
NIRCam	F115W & F335M (CH_4)	MEDIUM	4	10	4	1632
NIRCam	F140M (H_2O, CH_4) & F360M	MEDIUM	4	10	4	1632
NIRCam	F162M (ref for F140M) & F470N (H_2)	MEDIUM	4	10	4	1632

might be a binary system, which would account for at least 0.75 mag of its separation from the Y/T locus. Most recently, Cushing et al. (2021) used 0.7–1.7 μm HST spectroscopy and a new generation of models (the Sonora Bobcat models; Marley et al. 2021) to bolster the idea that WISE 1828+2650 is an unresolved binary consisting of roughly equal-mass objects with $T_{\rm eff} \sim 275$–350 K. However, there remain challenges with the model ages (<1 Gyr for a single object) and the subsolar values of [M/H] ~ -0.5 and [C/O] ~ -0.6 required to fit the existing data (Cushing et al. 2021).

With the expectation that JWST would help resolve these theoretical difficulties, we set out a program of imaging and spectroscopy, in particular in the key 3–10 μm region. The JWST NIRCam imaging data permit a search for faint companions at separations and sensitivity levels not previously possible, as well as anchoring the fluxes of the the higher spectral resolution NIRSpec data. The spectroscopy provides critical diagnostics of physical conditions, composition, the presence or absence of clouds, and surface gravity in the 3–5 μm region where Y dwarfs emit most of their energy.

This paper describes NIRCam imaging in six filters spanning 1–5 μm undertaken by the NIRCam Guaranteed Time Observation (GTO) team under PID#1189. Companion papers will give results from NIRSpec and MIRI spectroscopy, as well as from a deep NIRISS search for a close companion. Section 2 describes the observations and Section 3 the data reduction procedures and results. Section 4 addresses the search for and limits to the presence of a close companion to WISE 1828+2650, while Section 5 presents fits to the spectral energy distribution of WISE 1828+2650 and estimates of derived physical parameters. The paper ends with a search for wide-field companions (Section 6) and concluding remarks.

2. Observations and Data Reduction

Table 1 describes the observing parameters for this program, using the long- and short-wavelength modules of NIRCam to observe WISE 1828+2650 simultaneously in a combination of narrow, medium, and wide filters between 0.9 and 4.7 μm. Data were obtained on 2022 July 28 UTC. The NIRISS full-frame imager was used to obtain a long exposure in the F480M filter in a deep search for a close companion. The NIRISS results will be presented separately, but the photometry at that wavelength is presented here for comparison with models. NIRSpec and MIRI spectroscopy were also obtained at this time and are discussed separately.

NIRCam images in the six wavelength bands and the single NIRISS band were downloaded from the Mikulski Archive for Space Telescopes (MAST) at the Space Telescope Science Institute, specifically the "...i2d.fits" files, which are the result of mosaicking the four dither positions obtained at each wavelength. The specific observations analyzed can be accessed via 10.17909/jxva-9x26. Figure 1 shows a three-color, full-frame NIRCam image of the field around WISE 1828+2650 and is composed of images obtained at F162M (blue), F335M (green), and F470M (red), with a close-up around the position of WISE 1828+2650. Only one object in the frame appears with the highly red color characteristic of a cool Y dwarf.

3. Analysis

The values listed here use image files created on 2022 November 11 using calibration software version 11.16.14 and photometric reference data from jwst_nircam_photom_0114.fits.

3.1. Photometry

Table 2 shows the results of standard aperture photometry using the astropy/photutils package (Astropy Collaboration et al. 2013, 2018, 2022; Bradley et al. 2020) with the image files created on 2022 November 11 and the calibration software version 11.16.14 with photometric reference data from jwst_nircam_photom_0114.fits. We selected an aperture size corresponding to 70% encircled energy and the appropriate aperture correction from the CRDS database.[16] The F090W filter was the weakest detection, with the total flux dependent on the selected aperture, due to the poorly defined point-spread function. For small apertures with encircled energy < 50%, the flux estimates in F090W were variable at the 20%–30% level. Beyond encircled energy of 50%, the flux estimates were consistent at the 10% level, shown in the total uncertainty in Table 2. We adopted a large radius of 9.25 pixels encircling 85% of the total energy for the F090W filter. We also obtained photometry using the NIRISS imager in full-frame mode (Willott et al. 2022) using the same procedure as described above.

Figure 2 shows the JWST results along with previous data from Spitzer, WISE, HST, and Keck (Kirkpatrick et al. 2011, 2019; Leggett et al. 2015; Cushing et al. 2021). WISE 1828+2650 is detected at high signal-to-noise (S/N) in all filters with statistical uncertainties of just a few percent. However, we adopt a higher level of uncertainty for the absolute calibration in the model fitting. Successive MAST releases of these data from 2022 August to November have shown significant variations in the absolute calibration of the NIRCam filters used here. We adopt a uniform 10% uncertainty for the absolute photometric calibration in all filters.

We note the consistency between the JWST data and previous observations, although different passbands can be expected to yield significant differences, given the highly structured nature of the SED of cool BDs. The close agreement between multiple facilities at the wavelengths of peak emission around 4–5 μm is consistent with the general lack of variability in the brightness of WISE 1828+2650. H. Brooks et al. 2023, (in preparation) investigated the variability of several hundred cold BDs observed in the Kirkpatrick et al. (2021) astrometric

[16] https://jwst-crds.stsci.edu/

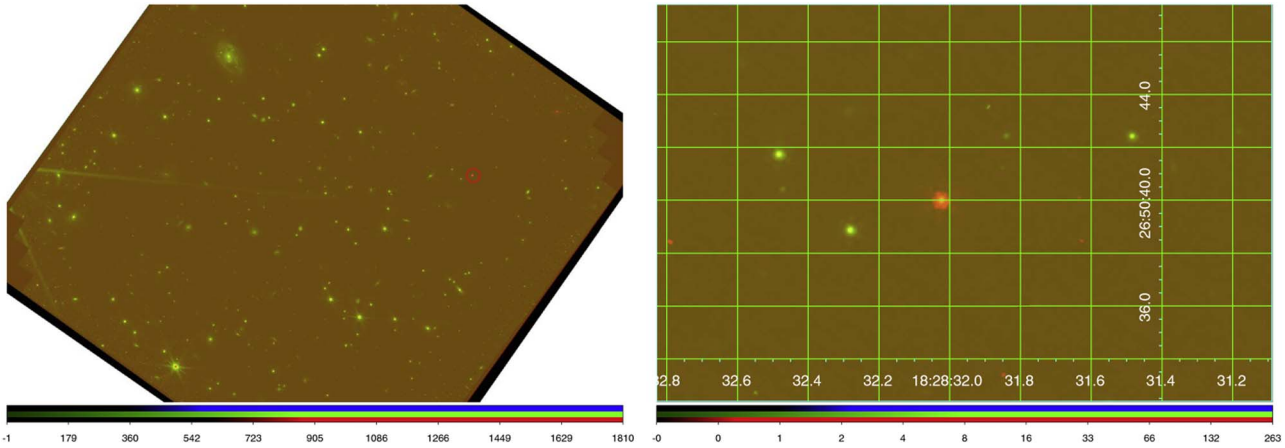

Figure 1. left) A color-composite image of three NIRCam filters, F162M, F335M, and F470N, showing one extremely red object at the expected position of WISE 1828+2650. (right) A zoom-in on the position of WISE 1828+2650.

Table 2
NIRCam Photometry

Filter	$F_\nu(\mu$ Jy)[a]	Magnitude
F090W	$0.078 \pm 0.005(0.015)$	26.16 ± 0.20
F115W	$0.311 \pm 0.005(0.03)$	24.39 ± 0.10
F162M	$1.29 \pm 0.009(0.13)$	22.25 ± 0.10
F335M	$2.41 \pm 0.013(0.24)$	20.23 ± 0.10
F360M	$34.2 \pm 0.05(3.4)$	17.19 ± 0.10
F470M	$340.4 \pm 0.62(34)$	14.16 ± 0.10
F480M[b]	$326 \pm 0.14(32)$	14.21 ± 0.10
J (1.25 μm)	0.65 ± 0.23	23.48 ± 0.23
H (1.65 μm)	0.83 ± 0.21	22.73 ± 0.13
K (2.16 μm)	0.27 ± 0.08	23.48 ± 0.36
Spitzer/IRAC (3.55 μm)	48.1 ± 1.0	16.92 ± 0.02
Spitzer/IRAC (4.55 μm)	335.5 ± 6.71	14.32 ± 0.02
WISE W2 (4.62 μm)	310 ± 14	14.35 ± 0.05

Notes.
[a] First quoted uncertainty reflects only photometric accuracy based on aperture photometry. Values in parenthesis include an average 10% calibration uncertainty at all wavelengths estimated from the average of successive iterations of the calibration values (PHOTMJYSR and PIXAR_SR) available at MAST. The values listed here use image files created on 2022 November 11 using calibration software version 11.16.14 and photometric reference data from jwst_nircam_photom_0114.fits. Values below the solid line come from ground and space missions as given in Liu et al. (2016), Martin et al. (2018), and Kirkpatrick et al. (2019, 2021).
[b] Observation obtained using the NIRISS instrument.

program using Spitzer. For WISE 1828+2650, they found a limit of 3% (3σ) to the variability in IRAC Ch2 ([4.5]) in 28 observations spanning almost 8 yr. A model fit based on the cloudless Sonora Bobcat models (Marley et al. 2021) is also plotted and will be discussed in Section 5.

3.2. Astrometry

As described in Kirkpatrick et al. (2019), WISE 1828+2650 has a high proper motion ($\sim 1'' \, \mathrm{yr}^{-1}$), mostly in R.A., and a parallax corresponding to a distance of 9.93 ± 0.23 pc. The values listed in Table 3 were used to establish the pointing of the NIRCam, NIRSpec, and MIRI observations in this program.

The F360M image was used to obtain the position of WISE 1828+2650. The high signal-to-noise ratio in this filter would imply a nominal positional accuracy of $\mathrm{FWHM}/(2 \times \mathrm{S/N}) < 5$ milliarcseconds (mas), where FWHM is the full width at half maximum of the point-spread function. We calculated both center-of-mass and 2D Gaussian fits to obtain the image centroid, which yielded a nominal accuracy of <0.1 pixel or <6 mas. Information in the FITS header was used to convert the pixel location into celestial coordinates (J2000, 2022.5699) as given in Table 3.[17]

A comparison of the NIRCam positions of 31 unsaturated, proper-motion-corrected Gaia stars ($20 \, \mathrm{mag} > \mathrm{Gmag} > 14$ mag) across the $4' \times 4'$ field showed a small offset on the order of the measurement uncertainty, with a dispersion of $(\Delta\alpha, \ \Delta\delta) = 10 \pm 10, \ 7 \pm 6)$ mas, demonstrating that the reference frame is accurate to ~5–10 mas. However, Figure 3 shows that there remain some coherent distortions across the field of view.

The predicted position of WISE 1828+2650 was calculated at the JWST epoch incorporating stellar parallax (Smart & Green 1977) using the rectangular coordinates of JWST's location in the Solar System as given in the FITS header (reversed to give the coordinates of the Sun). The uncertainty in the F360M position is the combination of the centroid uncertainty and the uncertainty in the reference frame derived from the Gaia stars, ±2 mas, for a combined uncertainty of ±4.4 mas. The difference in the predicted versus observed positions is within the uncertainties derived from a Monte Carlo run in which the Kirkpatrick et al. (2021) values were varied according to their quoted uncertainties. The Monte Carlo distribution yielded uncertainties at the JWST epoch of 6.4 mas in R.A. and decl. The predicted–JWST position difference is consistent with the existing parallax and proper motion values for WISE 1828+2650.

4. Search for Close Companions

4.1. Near-IR Observations

Previous observations with Keck and HST revealed no evidence for multiplicity at the level of 0.″1 (Beichman et al. 2013), corresponding to orbital separations of >1 au for equal-brightness components. However, the Keck observations were done with the $40 \, \mathrm{mas \, pixel}^{-1}$ wide-field camera mode with a

[17] The astrometric distortion correction in the MAST processing used the file crds://jwst_nircam_distortion_0158.asdf.

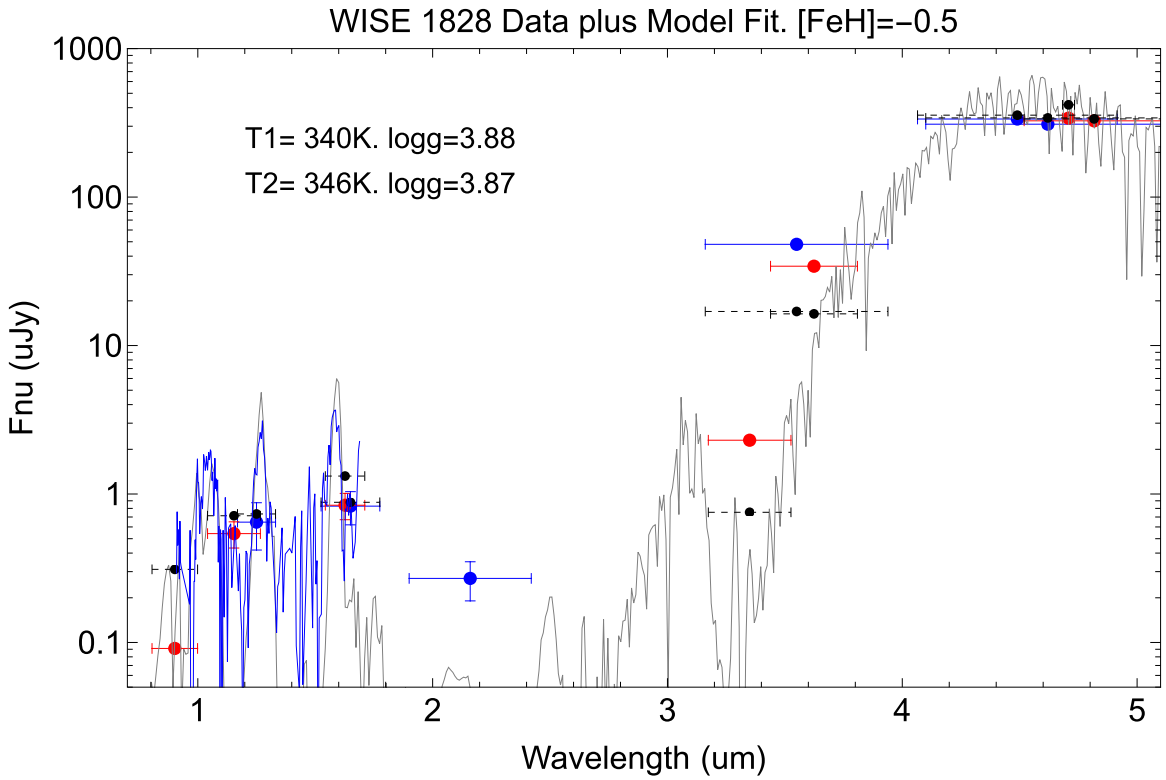

Figure 2. The figure shows a combination of the new JWST photometry (large red circles), previous ground-based and space-based observations (large blue circles) (Kirkpatrick et al. 2011, 2019; Leggett et al. 2015), and in the 1–2 μm region the HST spectrum (Cushing et al. 2021, thin blue line). Horizontal bars denote the widths of the various filters. As discussed further in Section 5, we also plot as a thin gray line a cloudless Sonora (Bobcat) spectrum smoothed to $R \sim 3000$ for the best-fitting, binary-object solution (Table 4). The black circles with dashed lines denote predicted fluxes as integrated over the relevant passbands for each filter (Marley et al. 2021).

Table 3
NIRCam Astrometry of WISE 1828

Observatory	Epoch (MJD)	R.A. R.A. (Equinox = J2000)	Decl. (Equinox = J2000)	Parallax (mas)	$\mu_{\rm R.A.}$ (mas yr^{-1})	$\mu_{\rm decl.}$ (mas yr^{-1})
Spitzer[a]	57094.09	277.131096 (±2 mas) $18^{\rm h}28^{\rm m}31\overset{\rm s}{.}463$	26.844069(±2 mas) $+26°50'\ 38\overset{''}{.}65$	100.3 ± 2	1016.5 ± 0.8	169.3 ± 0.8
JWST (predicted)	59788.5143	277.1334156 (±6 mas) $18^{\rm h}28^{\rm m}32\overset{\rm s}{.}020$	26.8444348 (±6 mas) $+26°50'\ 39\overset{''}{.}965$			
JWST (F360M)	59788.5143	277.1334164 (±10 mas) $18^{\rm h}28^{\rm m}32\overset{\rm s}{.}020$	26.8444334 (±10 mas) $+26°50'\ 39\overset{''}{.}960$			
ΔSpitzer-JWST(pred)		$-7\overset{''}{.}45$	$-1\overset{''}{.}32$			
ΔJWST (Pred-Obs)		2.5 ± 12 mas	−5.1 ± 8.2 mas			
Gaia-JWST differences[b] (mas)		10.4 ± 10.2 (1.8)	6.8 ± 5.1 (0.9)			

Notes.
[a] Kirkpatrick et al. (2019).[2] Absolute astrometric accuracy estimated by measurements of nearby Gaia stars.
[b] Difference in positions between 31 proper-motion-corrected Gaia stars and their JWST values. The value in parenthesis is the σ_mean for the sample and represents an estimate of the overall precision of reference frame.

typical resolution of $\sim 0\overset{''}{.}16$. New Keck observations were obtained 2022 September 8 UT with NIRC2 behind the laser guide star adaptive optics system (Wizinowich et al. 2000) in the narrow-field camera mode with a pixel scale of $0\overset{''}{.}009942$.

Observations of WISE 1828+2650 were made in the H filter ($\lambda_o = 1.633$; $\Delta\lambda = 0.296$ μm) with an integration time of 300 s per frame in a standard three-point dither pattern that is used with NIRC2 to avoid the noisier lower-left quadrant. The transparency and seeing during the night were highly variable and not all frames detected the BD. A total of 12 frames at 300 s each were acquired, yielding a total on-source integration time of 3600 s.

The science frames were flat-fielded and sky-subtracted. The flat fields were generated from a median average of dark subtracted flats taken on-sky. The flats were normalized such that the median value of the flats is unity. The sky frames were generated from the median average of the dithered science frames; each science image was then sky-subtracted and flat-fielded. The reduced science frames were combined into a single combined image using a intra-pixel interpolation that

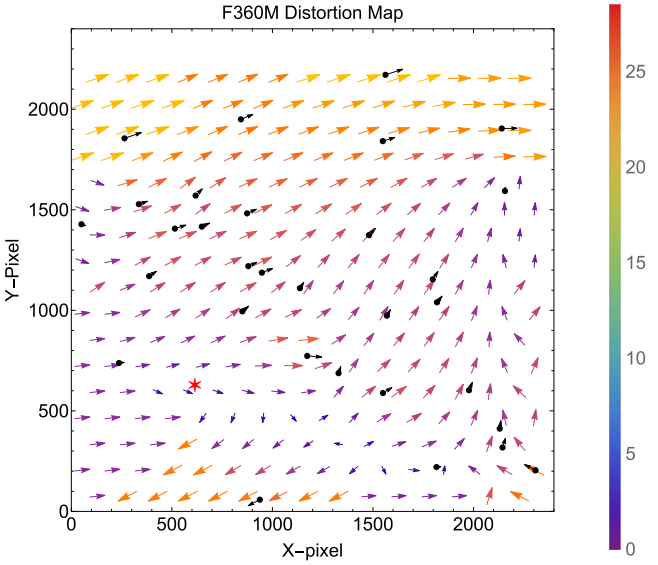

Figure 3. Differences in the positions of 31 Gaia DR3 stars (selected for negligible parallactic motions and corrected for proper motion) relative to the positions observed by JWST in F360M. Individual Gaia stars are shown as black symbols, with the arrow showing the difference in pixels (63 mas), scaled by a factor of 200 for visibility. The position of WISE 1828+2650 is shown as a red star. The colors in the image and the color bar encode the magnitude of deviation in mas. The maximum Gaia–JWST difference is 27 mas, with an average of 10 mas and dispersion of 10 mas.

conserves flux, shifts the individual dithered frames by the appropriate fractional pixels, and median-coadds the frames. The final resolutions of the combined dithers was determined from the full width at half maximum of the point-spread functions: 7.1 pixels = 0.″071.

The sensitivity of the final combined AO image was determined by injecting simulated sources azimuthally around the primary target every 20° at separations of integer multiples of the central source's FWHM. The brightness of each injected source was scaled until standard aperture photometry detected it with 5σ significance. The resulting brightness of the injected sources relative to WISE 1828+2650 set the contrast limits at that injection location. The final 5σ limit at each separation was determined from the average of all of the determined limits at that separation, and the uncertainty on the limit was set by the rms dispersion of the azimuthal slices at a given radial distance. The Keck data have a sensitivity close-in of $\Delta H \approx 1.5$ mag at 0.″071; the final sensitivity curve for the Keck image is shown in Figure (4). No close-in stellar companions were detected, and the FWHM of the WISE 1828+2650 is consistent with the brighter nearby star to the southeast (Gaia DR3 4585337218702066560). WISE 1828+2650 is $\Delta H = 3.4 \pm 0.2$ mag fainter than Gaia DR3 4585337218702066560.

The H-band magnitude of WISE 1828+2650 as measured by the Keck data is $H = 22.9 \pm 0.2$ mag. Using the JWST F162M filter as a proxy for the H-band filter, this measurement is consistent with the infrared photometry determined directly from the JWST images (see Table 2).

4.2. NIRCam Observations

Although the aperture of JWST is smaller than that of Keck, JWST offers a highly stable point-spread function (PSF) and much greater sensitivity at wavelengths where cold BDs are brightest. For the JWST data reported here, the best combination of spatial resolution and S/N in the JWST data comes in the F360M filter. A simple Gaussian fit of the image of WISE 1828+2650 compared to fits of two nearby stars shows no evidence for extent: FWHM(WISE 1828+2650) = 0.″150 ± 0.″001 compared with 0.″153 ± 0.″001 and 0.″150 ± 0.″001 for the two stars.

We explored the data further by constructing realistic models of the PSF and searching for a potential companion at all separations within 0.″25. Anderson & King (2000) and Anderson (2016) developed a novel technique applicable to multiple instruments on HST where they construct an "effective" PSF (ePSF) from bright single stars within a given image. The ePSF is intended to describe the contemporaneous realization of the theoretical PSF on the detector pixels given the wave front during the observation. They build the ePSF first by identifying a sample of many bright stars in the image that appear to be singles and without contamination from cosmic rays or other stars. These stars are all centered at various positions within their peak pixel, giving many samplings of the distribution of flux of the center of the PSF. The initial ePSF is then generated by interpolating each PSF by the factor of user-defined oversampling and taking the median. Then, an iterative process begins, comparing the ePSF to all stars in the sample, evaluating the median residual, and adding that on to the ePSF model. For our case, we generated an ePSF model 4 × oversampled, as recommended in Anderson (2016), after 20 iterations of the ePSF calculation, over 9 × 9 detector pixels. This analysis was performed using publicly available PSF building tools from the Python package photutils (Bradley et al. 2020).

We chose the F360M data to perform this analysis, as the number of bright sources in the F470N data was small, which limits the production of a reasonable ePSF model. Also, the diffraction limit in F470N is 30% larger than in F360M, limiting the sensitivity to close companions. We also avoid the F335M filter due to the low signal-to-noise ratio of WISE 1828+2650. Of the four pointings, two had reliable data for WISE 1828+2650 without nearby cosmic rays or bad pixels contaminating its flux. Within each integration, we constructed a separate ePSF model from 57 and 63 separate stars (integrations #2 and #4, respectively), excluding WISE 1828+2650 from the sample.

We then made a double-PSF fitting code that takes a cutout array of the data as input (here, a 9 × 9 pixel array centered around WISE 1828+2650) and then fits the best-fit binary model using the ePSF, an approach similarly implemented on HST (De Furio et al. 2019). We use the Python module PyMultiNest (Buchner et al. 2014) that performs the Nested Sampling Monte Carlo analysis using MultiNest (Feroz et al. 2009) to derive the best-fit binary ePSF model to the data, by maximizing our chi-squared likelihood statistic. Our model consists of six parameters: the x and y center of the primary, the flux normalization of the primary, the separation between the centers of the primary and secondary, the position angle of the center of the secondary relative to the primary, and the difference in magnitude between the secondary and primary. We define flat priors with $-1.5 \leqslant x_{\rm cen} \leqslant 1.5$, $-1.5 \leqslant y_{\rm cen} \leqslant 1.5$, 0.0 < flux normalization < 40.0, 0.01 ⩽ separation ⩽ 4.0 pixels, 0.0 ⩽ position angle < 360.0, and 0.01 ⩽ difference in magnitude ⩽ 6.0 mag.

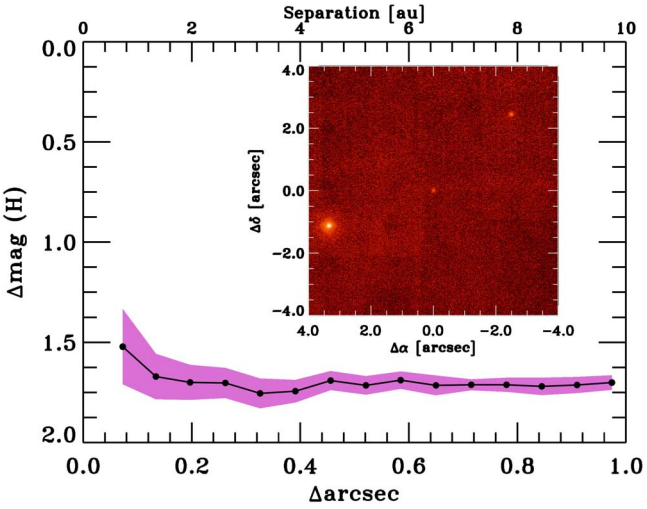

Figure 4. Keck NIR AO imaging and sensitivity curve for WISE 1828+2650 taken in the *H* filter. We can recover a companion at a contrast of ∼1.5 mag relative to the BD at separations greater than 0.″071. *Inset:* Image of the central portion of the NIRC2 image.

For both images of WISE 1828+2650 in F360M in question, the code converges to the edge of the prior in separation (four pixels) and approaching that in difference in magnitude (5.6 and 5.8 mags in each). If instead we force the code to fit within the core of the PSF ($0.01 \leqslant$ separation $\leqslant 2.0$ pixels) and exclude wide separations, the best fit converges to $0.14^{+0.04}_{-0.03}$ pixels in separation and $\Delta\mathrm{mag} = 2.44^{+0.34}_{-0.36}$ in Frame #2, and $0.28^{+0.13}_{-0.06}$ pixels in separation and $\Delta\mathrm{mag} = 3.06^{+0.74}_{-0.68}$ in Frame #4 (errors are the 68% confidence interval). See Figure 5 for the comparison of our binary-PSF model to the data.

However, our binary-PSF-fitting code will always find a best-fit binary solution regardless of whether a true binary is present. If the object in question is a single point source, the code will either fit a companion to the brightest residuals in the background (e.g., the four pixels in separation and Δmag ∼ 5.5–6 mag initial fit) or to the residuals in the core of the source, as models are limited by photon noise and have uncertainty (e.g., the resulting best fit when forced to fit a companion at separations < 2 pixels).

In order to determine whether we can recover a companion with these values, we constructed many artificial binaries from the ePSF models at various separations and differences in magnitude with the same signal-to-noise ratio as our F360M data. Then, we ran our double-PSF fitting code and a modified version that just fits a single PSF (three variables: x_{cen}, y_{cen}, and flux normalization) on those same artificial binaries. PyMultiNest also calculates the evidence of the model in question by integrating over the posteriors. Trotta (2008) define a difference of five in the log-evidence between two models as being strong evidence for one model over another (with a probability of 0.993 that the higher-evidence model is preferred). For a given companion at some separation and difference in magnitude, we compare the log-evidence of the binary-PSF model to that of the single-PSF model.

In Figure 6, we show the log-evidence difference between the binary- and single-ePSF model fits based on separation and difference in magnitude of our artificial binaries. We define our sensitivity as the point where the difference in log-evidence between the binary- and single-PSF models equals five. With our binary fitting tool and ePSF models, we can resolve companions down to ∼0.8 F360M pixels (0.″05) in separation for an equal-brightness companion and are sensitive to companions at $\Delta\mathrm{mag} = 2.5$ beyond two F360M pixels (0.″126). See Figure 7 for the posteriors for a fit to a binary at 1.25 pixels in separation and $\Delta\mathrm{mag} = 1.0$ and 3.5 . For the

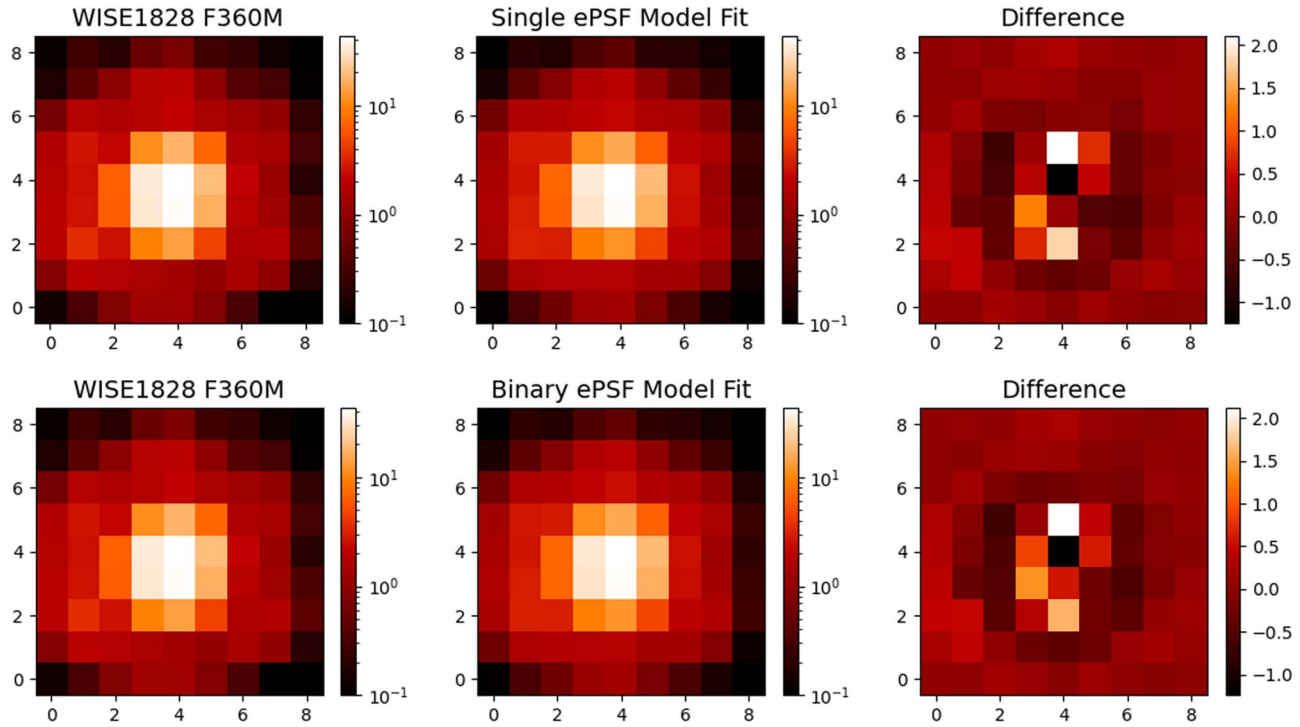

Figure 5. Top row: WISE 1828+2650 cutout in the F360M filter on the left, ePSF single model in the center, and residuals on the right. Bottom row: WISE 1828 +2650 cutout in the F360M filter on the left, ePSF binary model in the center, and residuals on the right. Units are in DN/s, and the axes are in detector pixels (0.″063 pixel^{-1}). We used the level 2 pipeline product *cal.fits files to perform this analysis.

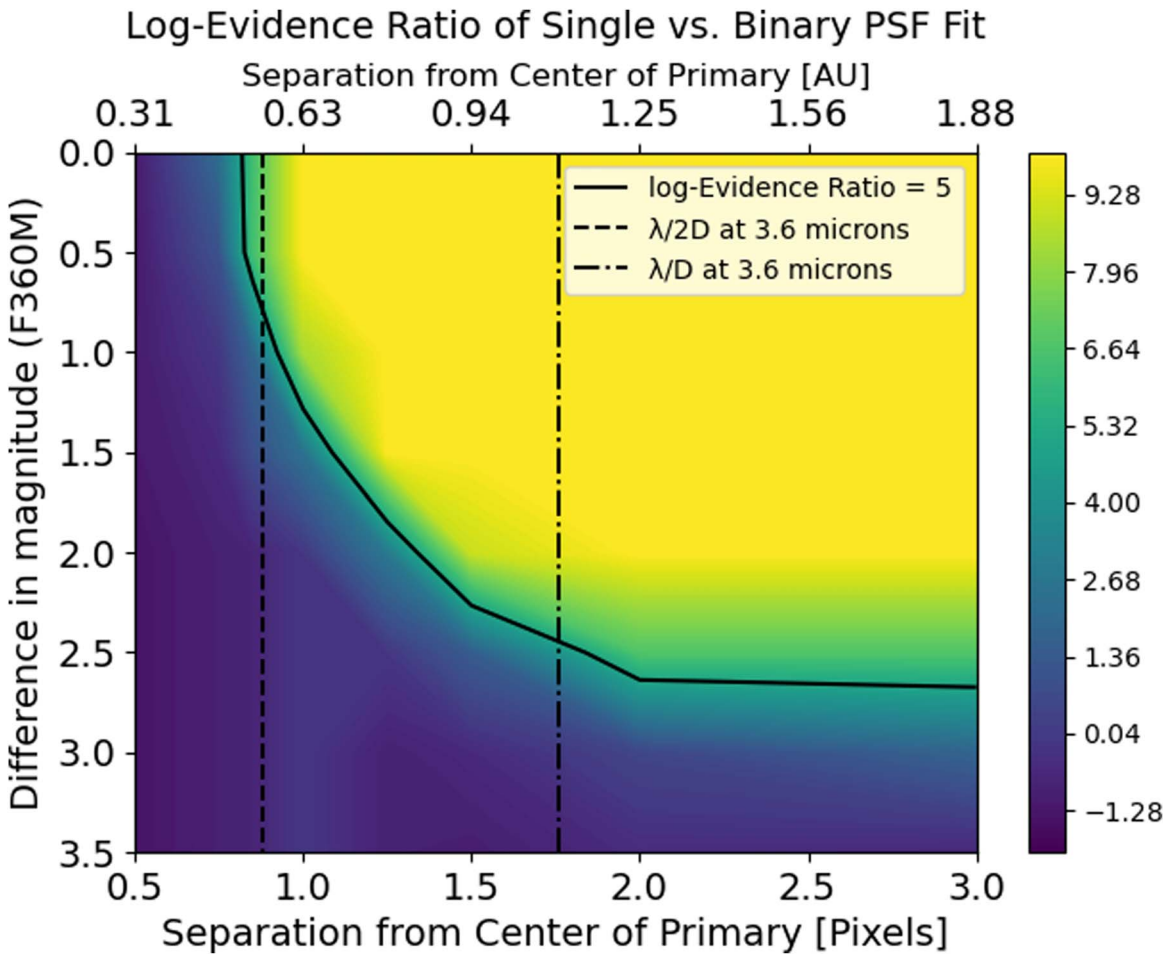

Figure 6. Shown is the difference in log-evidence between the binary-PSF model and single-PSF model performed on artificial binaries, made from the ePSF models. The threshold for strong evidence of the binary model fit over the single model fit is shown with a solid line (corresponding to a difference of five). The diffraction limit and half the diffraction limit at 3.6 μm are shown for comparison as the vertical dashed–dotted and dashed lines, respectively.

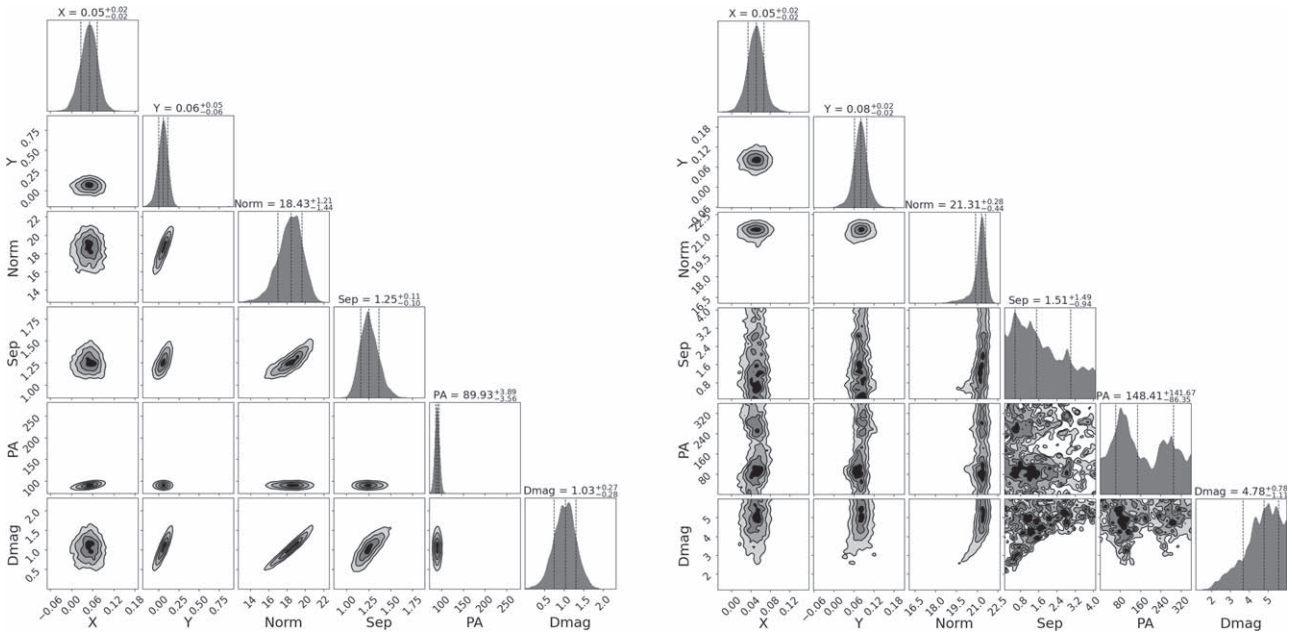

Figure 7. Binary model parameters from the recovery of a companion injected at 1.25 pixels in separation (Sep), a position angle (PA) of 90°, and a contrast (Dmag) of 1.0 (left) and 3.5 (right) mag relative to the primary. These artificial binaries were constructed from empirical PSFs of NIRCam in the F360M filter. *X* and *Y* are the central pixel coordinates of the primary, and Norm is the flux normalization of the primary.

Δmag = 3.5 companion, the parameters (separation, position angle, and difference in magnitude) are unconstrained.

In addition, we fit a single-PSF model to the WISE 1828+2650 data set. The difference in log-evidence between the single- and binary-PSF models is 3.5, i.e., less than the threshold for a detection. In Figure 5, we show both the single- and binary-PSF models compared to the data, demonstrating how the binary fit does not significantly improve the residuals. Therefore, we are confident that the best-fit binary model solution to WISE 1828+2650 in the F360M filter is not a true detection of a companion, and that we can rule out an equal-mass companion beyond 0.5 au and a Δmag = 2.5 companion beyond 1.25 au. Fainter companions at larger separations can also be ruled out, although these would not help resolve the problem of excess brightness of WISE 1828+2650 relative to model predictions. Such models generally require an equal-mass system, as discussed below (Section 5).

The incidence of binarity among BDs is generally low, 10%–30%, compared with higher-mass stars (Burgasser et al. 2007; Raghavan et al. 2010). While less is known about the multiplicity of the coldest T/Y BDs, there is evidence that the incidence of binarity may be even lower than for warmer BDs, with Opitz et al. (2016) failing to find any companions in the range of 0.5–2 au among the five Y dwarfs they examined with AO imaging. Similarly, Fontanive et al. (2018) estimated a companion frequency <10% for T-Y dwarfs with separations tightly peaked at 3 au, e.g., Luhman 16 AB (Luhman 2013). However, it should be noted that separations $\leqslant$3 au have not been explored well. If indeed WISE 1828+2650 is a binary as inferred from the spectral modeling presented by Cushing et al. (2021), then high-resolution JWST NIRSpec spectra may reveal a double-lined system, given an appropriate orbital plane inclination. Furthermore, two 5–10 M_J objects orbiting at 0.5 au would have a period of 3–5 yr and a typical orbital velocity of $\sim$5 km s^{-1}, which might be discernible in multiple epochs of high-S/N spectra to yield masses for the two objects.

5. The Spectral Energy Distribution and Model Fits

The broad wavelength coverage of JWST NIRCam photometry from 1 to 5 μm is ideal for characterizing the spectral energy distribution (SED) and inferring the bulk atmospheric properties of BDs. We include 13 ground- and space-based photometric points (i.e., Table 2) in our spectral energy distribution fitting. We considered a number of models for this comparison: Sonora Bobcat and Cholla (Marley et al. 2021), ATMO (Phillips et al. 2020) chemical-equilibrium (CEQ) models, ATMO chemical nonequilibrium models with strong vertical mixing (CNEQ-strong), and the Linder et al. (2019) models. We selected cloudless Sonora models[18,19] as the most up-to-date, compared, e.g., with older COND models, or the recent Linder et al. (2019) models, which are limited to low-mass objects (<2 M_J). The Sonora Cholla models do not go to sufficiently low temperatures for this study, and the ATMO 2020 models gave similar results but with higher reduced chi-squares than the Sonora Bobcat models.

We defer discussion of the new Leggett et al. (2021) models to a companion paper on the NIRSpec low- and high-resolution spectroscopy (B. Lew et al. 2023, in preparation). Leggett et al. (2021) noted that their new model failed to fit the total luminosity of WISE 1828+2650 as a single object and assumed an equal-mass binary.

We used the Sonora model grid that comprises temperatures from 200 to 600 K, gravities from log(g) of 3.0–5.5 ms^{-2}, and metallicities [M/H] from −0.5 to 0.5. The ATMO model grid assumes an atmosphere with solar metallicity and spans a range of temperature from 100 to 900 K and of gravity from $10^{2.5}$ to $10^{5.5}$ cm s^{-2}. The ATMO chemical nonequilibrium models with strong vertical mixing assume an eddy diffusion coefficient of 10^6 cm^2 s^{-1} at a gravity of $10^{4.5}$ cm s^{-2} and decreases with higher gravity (see Figure 1 in Phillips et al. (2020). We linearly interpolated the models to construct a model spectra grid with a smaller spacing in temperature, gravity, and metallicity. We adopt a distance of 9.93 pc reported by Kirkpatrick et al. (2019).

In the model-fitting process, we examined two cases: a single object or a binary with different temperatures. For the SED fitting, we performed the least-squares fit to the 13 photometric points. For the binary case, we require the two objects to share the same age and metallicity. To enforce the equal-age constraints, we first calculate the age based on the free parameters temperature T_1 and gravity g_1 of one component of the binary using the Sonora evolution model. We then calculate the expected gravity g_2 of the second component based on the calculated age and sampled temperature T_2 of this object. Therefore, both components of the binary share the same age, where g_2 is thus a derived value based on T_1, g_1, T_2, and M. We calculate the chi-squared values of the binary models over the grid of temperature, gravity, metallicity, and radius of the binary components. We use the bootstrapping method to estimate the uncertainties of the fitted parameters. With the bootstrapping method, we randomly resample the 13 photometric points for 10,000 times and refit the models to the resampled data points with the least-squares method. We then calculate the 99.7 percentile range of the fitted parameters as the 3σ confidence ranges, as shown in Table 4.

In Table 4 and Figure 8, we show the best-fit parameters and display the corner plots associated with the fits to show the correlation between the parameters in our SED fitting. In the binary case, the chi-squared map suggests that the primary shares a temperature ($\Delta T < 50$ K) similar to that of the secondary when both components have non-negligible radii (R_1 and $R_2 > 0$). We also calculate the combined radius, which is the square root of the sum of the two radii squared ($\sqrt{R_1^2 + R_2^2}$), for the binary case. The combined radius is moderately constrained, with a 99.7 percentile range of 1.15–2.83 R_J and a median value of 1.67R_J, where the best-fit radius of the single model is 1.67R_J. Both the single and binary fits favor effective temperature of around 330K, low metallicity ([M/H = −0.5]), and low gravity (log(g) = 4). However, the best-fit models suggest that the single model requires a lower-mass object (2 M_J), while the binary model requires two higher-mass objects ($\sim$4 M_J). Our single model has a lower reduced χ^2 than the binary model, although both are too high to adequately represent the data. We note that the best-fitted radius of 1.67 R_J in the single BD case may be unphysically large, and that an equal-temperature binary may be preferred in this case, as suggested in previous studies of WISE 1828+2650 (e.g., Beichman et al. 2013; Leggett et al. 2013, 2017; Cushing et al. 2021; Leggett et al. 2021)

A striking characteristic of the SED fits for both the single and binary cases is their predicted youth, with best-fit ages

[18] https://zenodo.org/record/1309035#.YwqSGbTMKUk
[19] https://zenodo.org/record/5063476#.YwqSTrTMKUk

Table 4
Spectral Model Fits to Photometry

	Primary				Secondary								
	$T_{\rm eff}$ (K)	log g (cgs)	Mass ($M_{\rm Jup}$)	Radius ($R_{\rm Jup}$)	$T_{\rm eff}$ (K)	log g (cgs)	Mass ($M_{\rm Jup}$)	Radius ($R_{\rm Jup}$)	Metallicity [M/H]	Age ($\times 10^9$yr)	Reduced χ^2	Degs. of Freedom	log ($L/L_\odot$)
Sonora Cloudless Models													
best-fit single	325	3.6	2	1.83					−0.5[a]	0.3	180	9	-6.49 ± 0.03
99.7% CI	309–405	3.0–5.5	0.6–13	1.1–2.0					−0.5	0.01–7			
best-fit binary	337	4.0	4.4	1.38	330	4.0	4.1	0.90	−0.5[a]	0.7	231	7	-6.49 ± 0.04
99.7% CI	316–413	3.0–4.8	0.6–20	0.4–2	268–395	3.5–4.8	0.6–20	0–2	−0.5	0.03–10			
ATMO Chemical-equilibrium Models													
best-fit single	300	4.0	3.7	2					0 (fixed)	1.0	256	10	-6.45 ± 0.06
99.7% CI	287–359	3.0–5.1	0.5–13	2–2					⋯	0.02–8.5			
best-fit binary	300	3.6	1.5	1.9	300	3.6	1.7	1.4	0 (fixed)	0.3	287	8	-6.36 ± 0.05
99.7% CI	279–400	3.0–4.8	0.5–20	0.4–2	279–400	3.0–4.8	0.5–20	0–2	⋯	0.02–10			
ATMO Chemical-nonequilibrium Models with Strong Mixing													
best-fit single	294	4.3	5.5	2.0					0 (fixed)	2.4	303	10	-6.46 ± 0.06
99.7% CI	259–359	3.0–5.0	0.5–11	2.0–2.0					⋯	0.02–9.9			
best-fit binary	270	4.0	4.2	2	270	4.0	4.2	2	0 (fixed)	2.1	320	8	-6.38 ± 0.09
99.7% CI	253–340	3.0–4.6	0.5–13	2–2	253–340	3.0–4.6	0.5–13	2–2	⋯	0.03–9.9			

Notes.[1] The fitted parameters and the corresponding 99.7% percentile ranges for the single- and binary-object cases. The mass, radius, and the secondary object's gravity are derived from the fitted parameters using the Bobcat evolution models.
[a] The fitted metallicity is at the lower bound of the metallicity grid.

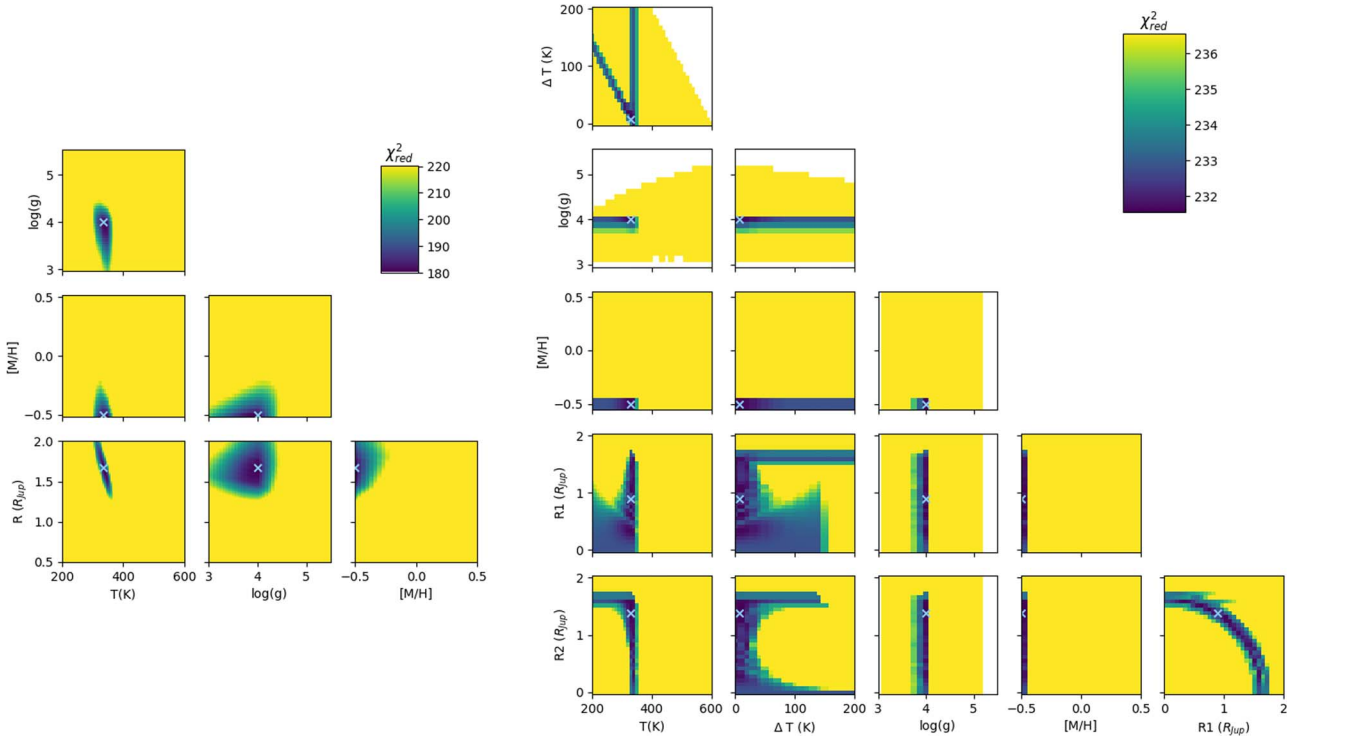

Figure 8. The reduced chi-squared maps of the photometry fitting results for both the single object case (left) and the binary case (right). Both models fitting results suggest WISE 1828+2650 has a temperature of around 330 K, low metallicity, and low gravity. The blue crosses mark the location with the lowest chi-squared values that are listed in Table 4. The white-colored regions in the plots are either outside of the considered temperature range (i.e., $T + \Delta T > 600$ K) or incompatible with the Bobcat evolution model grid.

between 0.30 and 0.7 Gyr, which is at odds with the likely dynamical age of WISE 1828+2650, although these young ages are not constrained well in our model. As previously noted (Beichman et al. 2014), WISE 1828+2650 is not associated with any known young cluster. This original conclusion is bolstered by application of the Banyan Σ tool[20] (Gagné et al. 2018), which puts the probability that WISE 1828+2650 is a field object at 99%, independent of its as yet unknown radial velocity. We expect WISE 1828+2650 to have an age in the 2–4 Gyr range, given its tangential velocity (Beichman et al. 2013), consistent with the mean age of 2.3 Gyr for a sample of BDs in the solar neighborhood (Dupuy & Liu 2017), contrary to our modeling of the SED.

Based on the best-fit models, we extrapolate the flux density beyond the observed wavelength regions and estimate the bolometric luminosity. The estimated bolometric luminosity has $\log(L/L_\odot)$ of around −6.5, as listed in Table 2. The bolometric luminosity of $\log(L/L_\odot) = -6.5$ is similar to the expected luminosity of a ∼400 K object at 1 Gyr. Our calculations indicate that the JWST broadband photometry covers about 16% of the bolometric luminosity, while the composite photometry comprising JWST, 2MASS, WISE, and Spitzer photometry accounts for around 55% of the bolometric luminosity.

The discrepancy between models for cold BDs at long and short wavelengths is well known (Beichman et al. 2014), with models that fit well at long wavelengths failing to fit at short wavelengths and vice versa. This failure is prominent in our fits to the WISE 1828+2650 data, independent of metallicity or multiplicity. In all cases, the models, which fit reasonably at 4–5 μm, fail badly at 1 μm, with the models being a factor of ∼2 brighter than observed at 1 μm. Another striking feature is that both the F335M and F360M data points sit significantly above the predictions, suggesting that the absorption in this part of the spectrum is less than expected. Further exploration of the possible temperature–pressure profile and atmospheric chemistry, such as those models in Leggett et al. (2021), is essential to understand the atmospheric processes that drive the long-standing challenges in fitting the flux at near-IR and mid-IR wavelengths.

The SED fits to new JWST observations using two independent sets of models leave us in the uncomfortable position of either accepting a single object much younger than expected dynamically, or a near-equal-mass binary system for which the NIRCam data finds no evidence at separations >0.5 au. Potentially, the NIRSpec's high-resolution spectroscopy may reveal a double-lined system, which might resolve this problem. However, whether WISE 1828+2650 turns out to be a double or not, Figure 2 and the high χ^2 values indicate significant deviations between the models and the emission of WISE 1828+2650.

At the fitted effective temperature of around 300 K, it is possible that sulfide, chloride, and water clouds form near or within the photosphere and affect the emission spectra (e.g., Morley et al. 2012, 2014b, 2014a). However, Cushing et al. (2021) SED fitting results with Morley et al. (2014b) cloud models at solar metallicity give a higher reduced chi square than that with Sonora Bobcat cloudless models with subsolar metallicity. Further exploring cloudy models under various atmospheric chemistries and metallicities is essential to understand the role of clouds in shaping the SED of WISE 1828+2650. It is possible that the rotation rate and observed

[20] www.exoplanetes.umontreal.ca/banyan/banyansigma.php?

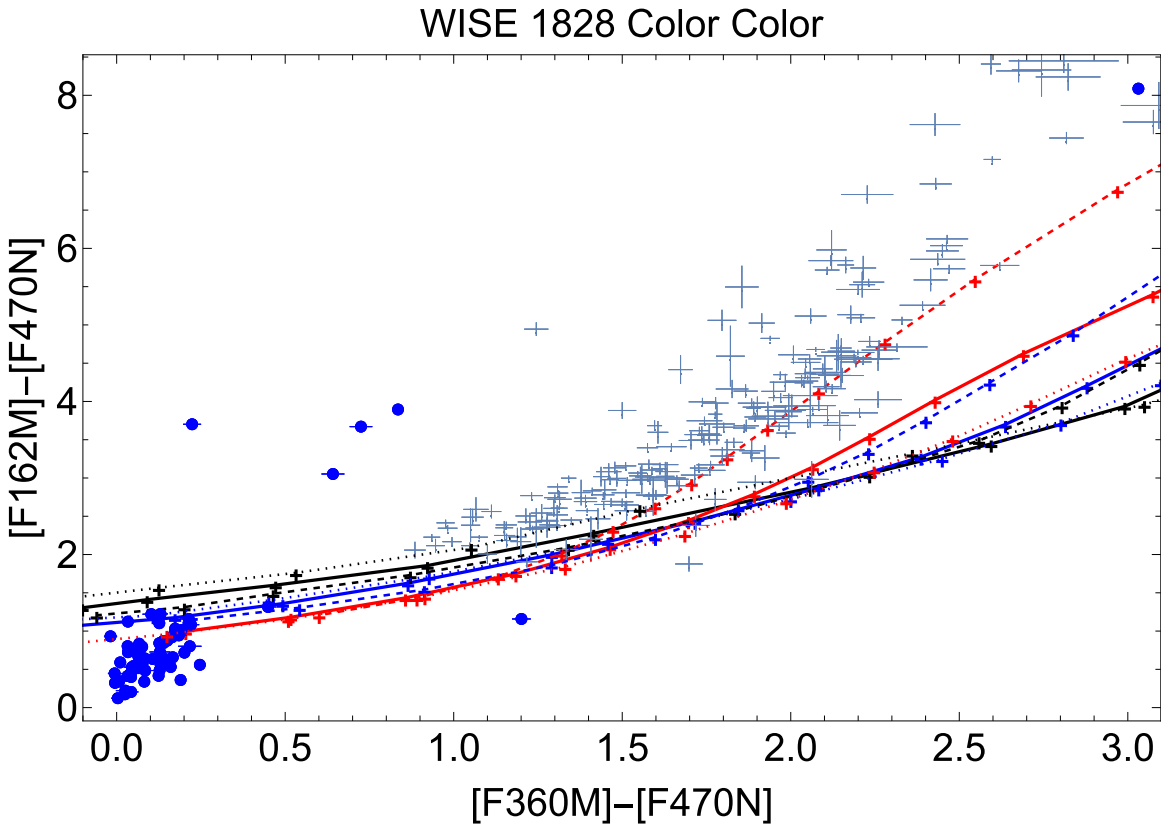

Figure 9. Color–color plot for point sources detected in all three bands seeded with a high-S/N detection in F360M. Blue circular symbols are sources in the WISE 1828+2650 field (WISE 1828+2650 is in the upper right corner), the light blue crosses represent the progression of BDs from Kirkpatrick et al. (2019) plotted in using *H*-band and Spitzer IRAC Ch1 and Ch2 similarly to the JWST filters. Visual examination of the F360M image shows that four JWST sources that lie above the BD locus are slightly extended, very red galaxies. The lines denote sequence of early-L to late-T dwarfs based on Sonora models (Marley et al. 2021). The colors denote values of log(*g*) (black, 3.0; blue, 4.0; red, 5.0). The line type denotes different values of [Fe/H] = (0, thick; −0.5, dashed; and +0.5, dotted).

inclination of WISE 1828+2650 cause significant luminosity deviations from a typical BD of similar temperature. Deviations as high as 20% have been estimated in comparing pole-on versus equator-on viewed BDs at high rotation rates (Lipatov et al. 2022), but it is currently unknown if this effect occurs for WISE 1828+2650. Important clues will come from the NIRSpec and MIRI spectroscopic observations spanning 1–12 μm at low and high resolutions, which are currently being analyzed.

6. A Search for Brown Dwarf Companions in the Entire Field

The large field of view and great sensitivity of NIRCam are two of the instrument's great strengths. In addition to searching for a close companion, we also looked for additional BD candidates that might or might not be associated with WISE 1828+2650. For example, Nonino et al. (2023) made a serendipitous discovery of a T dwarf ($T_{\rm eff} \sim 600$ K) at a distance of ∼0.5 kpc in a deep survey field adjacent to A2744.

We used the source catalogs provided by Level-3 processing from STScI for our six filters. We selected F360M unconfused point sources (with the "is_extended" flag set to FALSE and the nearest-neighbor distance $\geqslant 1''$) with S/N $\geqslant$ 10. To avoid unreliable sources that appear at the edges of the field due to having less than the full coverage of four dither positions, we selected objects only within the central $2' \times 2'$ of the final F360M image. We selected sources in the other five filters (S/N $\geqslant$ 5) in the same way and used the F360M objects as seeds for band merging using a radius of 0.″2. We adopted the catalog values of aperture photometry based on a 70% encircled value with pipeline-provided aperture correction. To enable a search for L, T, and Y BDs, we focused on filters optimized to find cold objects, requiring detections at F360M, F162M, and F470N. Figure 9 shows 63 sources meeting these criteria. Sources around 0.5>[F360M]–[F470N]>0 and 0 < [F162M]–[F470N] <2 mag are likely stars with spectral types as cool as M9 or galaxies (Pecaut & Mamajek 2013).[21]

Figure 9 shows only one object in the color space occupied by BDs, WISE 1828+2650 itself, in the upper right corner of the plot. Finally, there are four other red objects with colors around [F162M]–[F470N] >2 mag (Table 5). A sixth source with [F360M]–[F470N]∼1.2 lies below the BD locus and appears to be contaminated by confusion with a nearby object. Visual inspection and the measured FWHM of the four red objects shows two to be extended (Table 5). A more detailed examination of the images and comparison with the predicted WebbPSF[22] image size shows that #2 and #4 have respective FHWM values in the F360M image of 0.″23 and 0.″43, compared with other point sources in the field (0.″15 in the mosaicked images) and the WebbPSF FHWM of 0.″12–0.″13 (Table 5). A third, #5, may be slightly extended 0.″18. The other two, #1 and #6, are point-like or only very slightly extended. Source #3 is WISE 1828+2650. Extragalactic

[21] https://www.pas.rochester.edu/~emamajek/EEM_dwarf_UBVIJHK_colors_Teff.txt
[22] https://webbpsf.readthedocs.io/en/latest/

Table 5
Highly Red Sources in WISE 1828+2650 Field

Label	RA2000[a]	DEC2000[a]	F090W[b]	F115W[b]	F162M[b]	F335M[b]	F360M[b]	F470N[b]	FWHM[c]
1	277.138408(60.)	26.8286435(55.)	1.06 ± 0.00769	4.08 ± 0.00955	0.911 ± 0.00908	6.23 ± 0.0223	5.66 ± 0.0218	4.24 ± 0.0982	0.″15
	$18^h28^m33^s.22$	$26^d49^m43^s.12$	23.33 ± 0.0078	21.59 ± 0.0025	22.62 ± 0.011	19.2 ± 0.0039	19.15 ± 0.0042	18.92 ± 0.025	
2	277.160802(20.)	26.8420123(16.)	0.172 ± 0.00651	0.545 ± 0.00633	0.975 ± 0.00975	2. ± 0.0113	2.27 ± 0.0122	2.5 ± 0.0747	0.″23
	$18^h28^m38^s.59$	$26^d50^m31^s.24$	25.3 ± 0.04	23.78 ± 0.013	22.55 ± 0.011	20.43 ± 0.0061	20.14 ± 0.0058	19.5 ± 0.032	
3[d]	277.133408(26.)	26.8444326(4.3)	0.078 ± 0.005	0.311 ± 0.00446	1.29 ± 0.00857	2.41 ± 0.0132	34.2 ± 0.0511	340. ± 0.619	0.″15
	$18^h28^m32^s.02$	$26^d50^m39^s.96$	26.16 ± 0.20	24.39 ± 0.015	22.25 ± 0.0072	20.23 ± 0.0059	17.19 ± 0.0016	14.16 ± 0.002	
4	277.16172(24.)	26.8470549(26.)	0.0796 ± 0.00708	0.323 ± 0.00663	0.562 ± 0.00985	1.93 ± 0.0112	2.14 ± 0.012	2.55 ± 0.0752	0.″44
	$18^h28^m38^s.81$	$26^d50^m49^s.4$	26.14 ± 0.093	24.34 ± 0.022	23.15 ± 0.019	20.47 ± 0.0063	20.2 ± 0.0061	19.48 ± 0.032	
5	277.138946(24.)	26.8479253(5.9)	N/A	0.23 ± 0.0043	1.27 ± 0.00946	4.85 ± 0.0166	5.39 ± 0.0176	7.1 ± 0.098	0.″18
	$18^h28^m33^s.35$	$26^d50^m52^s.53$	N/A	24.71 ± 0.02	22.26 ± 0.008	19.47 ± 0.0037	19.2 ± 0.0035	18.36 ± 0.015	
6[e]	277.152549(430.)	26.8653645(380.)	2.42 ± 0.00887	3.94 ± 0.0116	9.63 ± 0.0276	6.41 ± 0.0218	2.34 ± 0.0225	4.31 ± 0.0968	0.″15
	$18^h28^m36^s.61$	$26^d51^m55^s.31$	22.44 ± 0.004	21.63 ± 0.0032	20.06 ± 0.0031	19.17 ± 0.0037	20.11 ± 0.01	18.91 ± 0.024	

Notes.
[a] Epoch 2022.5699, uncertainties in milliarcseconds in parentheses.
[b] Top line is flux density in μJy. Second line is corresponding Vega magnitude.
[c] Full width at half maximum in F360M. This is to be compared with the FWHM of the WebbPSF of 0.″17.
[d] Source is WISE1828+2650.
[e] Source to confusion with a nearby object.

objects with similar colors are being found in ongoing deep imaging programs and are suggestive of a new class of highly dust obscured galaxy (K. Hainline et al 2023, in preparation).

Figure 9 includes colors from a large sample of BDs from Kirkpatrick et al. (2021) using *H*-band and IRAC Ch1 and Ch2 as analogs for the JWST filters. The plot also includes the loci of six different Sonora BD models evaluated in the JWST filters and ranging in surface temperature, gravity, and metallicity: $300 < T_{\rm Eff} < 1700$ K, log(*g*) of (3,4,5), and [Fe/H] of (−0.5,0,+0.5). The comparison between the models and the Kirkpatrick sample shows the well-known problem that, as the BDs become cooler, the models have a progressively harder time fitting the data.

The conclusion of this search and visual inspection of the six JWST images is that there are no obvious cool BD candidates in the WISE 1828+2650 field, but that there are a significant number of galaxies.

7. Conclusion

This examination of the new 1–5 μm NIRCam data for WISE 1828+2650 has confirmed what has been previously known about this source. It remains among the reddest and most challenging of the Y dwarfs to fit using existing models. Both the high-S/N data at F360M and the data from the Keck telescope at 1.6 μm have failed to reveal a near-equal-mass companion beyond 0.5 au. If, as has been suggested, a binary system offers a better chance of fitting the photometric models, the companion must orbit very close to WISE 1828+2650 itself, i.e., <0.5 au. Such a companion might reveal itself through double lines in the spectroscopy. However, as described above, even the binary model fails to provide an improved fit to the existing photometric data. Further insights into the properties of this enigmatic object will come with the analysis of the NIRCam and MIRI spectroscopic data forthcoming shortly in other publications.

We must first acknowledge the many years of effort by thousands of scientists, engineers, and administrators who made JWST such a dramatic success, exceeding many of its most important requirements. This international collaboration should be an inspiration to us all. The NIRCam team at the University of Arizona and Lockheed Martin's Advanced Technology Center brought great skill, expertise, and dedication to realize the full power of this instrument. This work was supported by NASA through the JWST NIRCam project through contract No. NAS5-02195 (M. Rieke, University of Arizona, PI). T.R. would like to acknowledge the support of the NASA Science Mission Directorate under WBS 411672.07.05.05.03.01.

We wish to thank Davy Kirkpatrick for valuable discussions about WISE 1828. Some of the research described in this publication was carried out at the Jet Propulsion Laboratory, California Institute of Technology, under a contract with the National Aeronautics and Space Administration. M. De Furio benefited from support from JPL's Strategic University Research Partnership (SURP). Doug Johnstone is supported by NRC Canada and by an NSERC Discovery Grant. L.A. acknowledges support by the Canadian Space Agency under contract 9F052-170914/001/MTB.

Some of the data presented herein were obtained at the W. M. Keck Observatory, which is operated as a scientific partnership among the California Institute of Technology, the University of California and the National Aeronautics and Space Administration. The Observatory was made possible by the generous financial support of the W. M. Keck Foundation. The authors wish to recognize and acknowledge the very significant cultural role and reverence that the summit of Maunakea has always had within the indigenous Hawaiian community. We are most fortunate to have the opportunity to conduct observations from this mountain.

This work is based (in part) on observations made with the NASA/ESA/CSA James Webb Space Telescope. The data were obtained from the Mikulski Archive for Space Telescopes at the Space Telescope Science Institute, which is operated by the Association of Universities for Research in Astronomy, Inc., under NASA contract NAS 5-03127 for JWST. These observations are associated with program No. 1189.

This work was authored by employees of Caltech/IPAC under Contract No. 80GSFC21R0032 with the National Aeronautics and Space Administration.

ORCID iDs

Matthew De Furio https://orcid.org/0000-0003-1863-4960
Ben Lew https://orcid.org/0000-0003-1487-6452
Charles Beichman https://orcid.org/0000-0002-5627-5471
Thomas Roellig https://orcid.org/0000-0002-6730-5410
Geoffrey Bryden https://orcid.org/0000-0001-5966-837X
David Ciardi https://orcid.org/0000-0002-5741-3047
Michael Meyer https://orcid.org/0000-0003-1227-3084
Marcia Rieke https://orcid.org/0000-0002-7893-6170
Alexandra Greenbaum https://orcid.org/0000-0002-7162-8036
Jarron Leisenring https://orcid.org/0000-0002-0834-6140
Jorge Llop-Sayson https://orcid.org/0000-0002-3414-784X
Marie Ygouf https://orcid.org/0000-0001-7591-2731
Loic Albert https://orcid.org/0000-0003-0475-9375
Martha Boyer https://orcid.org/0000-0003-4850-9589
Daniel Eisenstein https://orcid.org/0000-0002-2929-3121
Klaus Hodapp https://orcid.org/0000-0003-0786-2140
Scott Horner https://orcid.org/0000-0001-9886-6934
Doug Johnstone https://orcid.org/0000-0002-6773-459X
George Rieke https://orcid.org/0000-0003-2303-6519
John Stansberry https://orcid.org/0000-0003-2434-5225
Erick Young https://orcid.org/0000-0002-6395-4296

References

Anderson, J. 2016, Empirical Models for the WFC3/IR PSF, Instrument Science ReportWFC3 2016-12
Anderson, J., & King, I. R. 2000, PASP, 112, 1360
Astropy Collaboration, Price-Whelan, A. M., Lim, P. L., et al. 2022, ApJ, 935, 167
Astropy Collaboration, Price-Whelan, A. M., Sipőcz, B. M., et al. 2018, AJ, 156, 123
Astropy Collaboration, Robitaille, T. P., Tollerud, E. J., et al. 2013, A&A, 558, A33
Beichman, C., Gelino, C. R., Kirkpatrick, J. D., et al. 2013, ApJ, 764, 101
Beichman, C., Gelino, C. R., Kirkpatrick, J. D., et al. 2014, ApJ, 783, 68
Bradley, L., Sipőcz, B., Robitaille, T., et al. 2020, astropy/photutils: 1.0.0, Zenodo, doi:10.5281/zenodo.4044744
Buchner, J., Georgakakis, A., Nandra, K., et al. 2014, A&A, 564, A125
Burgasser, A. J., Reid, I. N., Siegler, N., et al. 2007, in Protostars and Planets V , ed. B. Reipurth, D. Jewitt, & K. Keil (Tucson, AZ: Univ. Arizona Press), 427
Cushing, M. C., Kirkpatrick, J. D., Gelino, C. R., et al. 2011, ApJ, 743, 50
Cushing, M. C., Schneider, A. C., Kirkpatrick, J. D., et al. 2021, ApJ, 920, 20
De Furio, M., Reiter, M., Meyer, M. R., et al. 2019, ApJ, 886, 95
Dupuy, T. J., & Liu, M. C. 2017, ApJS, 231, 15

Feroz, F., Hobson, M. P., & Bridges, M. 2009, MNRAS, 398, 1601
Fontanive, C., Biller, B., Bonavita, M., & Allers, K. 2018, MNRAS, 479, 2702
Gagné, J., Mamajek, E. E., Malo, L., et al. 2018, ApJ, 856, 23
Kirkpatrick, J. D., Cushing, M. C., Gelino, C. R., et al. 2011, ApJS, 197, 19
Kirkpatrick, J. D., Gelino, C. R., Cushing, M. C., et al. 2012, ApJ, 753, 156
Kirkpatrick, J. D., Gelino, C. R., Faherty, J. K., et al. 2021, ApJS, 253, 7
Kirkpatrick, J. D., Martin, E. C., Smart, R. L., et al. 2019, ApJS, 240, 19
Leggett, S. K., Morley, C. V., Marley, M. S., et al. 2013, ApJ, 763, 130
Leggett, S. K., Morley, C. V., Marley, M. S., & Saumon, D. 2015, ApJ, 799, 37
Leggett, S. K., Tremblin, P., Esplin, T. L., Luhman, K. L., & Morley, C. V. 2017, ApJ, 842, 118
Leggett, S. K., Tremblin, P., Phillips, M. W., et al. 2021, ApJ, 918, 11
Linder, E. F., Mordasini, C., Mollière, P., et al. 2019, A&A, 623, A85
Lipatov, M., Brandt, T. D., & Batalha, N. E. 2022, MNRAS, 517, 2942
Liu, M. C., Dupuy, T. J., & Allers, K. N. 2016, ApJ, 833, 96
Luhman, K. L. 2013, ApJL, 767, L1
Marley, M. S., Saumon, D., Visscher, C., et al. 2021, ApJ, 920, 85
Martin, E. C., Kirkpatrick, J. D., Beichman, C. A., et al. 2018, ApJ, 867, 109
Morley, C. V., Fortney, J. J., Marley, M. S., et al. 2012, ApJ, 756, 172
Morley, C. V., Marley, M. S., Fortney, J. J., et al. 2014b, ApJ, 787, 78
Morley, C. V., Marley, M. S., Fortney, J. J., & Lupu, R. 2014a, ApJL, 789, L14
Nonino, M., Glazebrook, K., Burgasser, A. J., et al. 2023, ApJL, 942, L29
Opitz, D., Tinney, C. G., Faherty, J. K., et al. 2016, ApJ, 819, 17
Pecaut, M. J., & Mamajek, E. E. 2013, ApJS, 208, 9
Phillips, M. W., Tremblin, P., Baraffe, I., et al. 2020, A&A, 637, A38
Raghavan, D., McAlister, H. A., Henry, T. J., et al. 2010, ApJS, 190, 1
Smart, W. M., & Green, E. b. R. M. 1977, Textbook on Spherical Astronomy
Trotta, R. 2008, ConPh, 49, 71
Willott, C. J., Doyon, R., Albert, L., et al. 2022, PASP, 134, 025002
Wizinowich, P., Acton, D. S., Shelton, C., et al. 2000, PASP, 112, 315
Wright, E. L., Eisenhardt, P. R. M., Mainzer, A. K., et al. 2010, AJ, 140, 1868